Materials Letters 407 (2026) 140062

Contents lists available at ScienceDirect

Materials Letters

journal homepage: www.elsevier.com/locate/matlet

# (TiZrHf)$C_xN_y$/$Al_2O_3$ bilayer nanofilm enable enhanced solar selective absorption and thermal stability

Gaopeng Zou [a,b,c], Yuxi Qi [b,c], Zhiyuan Jing [a,**], Zhibin Zhang [a], Qianqian Wang [b,c,*], Zhenfeng Hu [a], Xiubing Liang [a,**], Baolong Shen [b,c]

[a] Defense Innovation Institute, Academy of Military Science, Beijing 100071, China
[b] School of Materials and Engineering, Jiangsu Key Laboratory for Advanced Metallic Materials, Southeast University, Nanjing 211189, China
[c] Ministry of Education Key Laboratory of Structure and Thermal Protection for High-Speed Aircraft, Southeast University, Nanjing 211189, China

ARTICLE INFO

*Keywords:*
Solar selective absorbers
Medium-entropy carbonitride
Plasmonic materials

ABSTRACT

Developing solar selective absorbers (SSAs) that combine high solar-thermal conversion efficiency with long-term thermal stability is critical for advancing solar energy technologies. Here, we report a novel SSA based on a (TiZrHf)$C_xN_y$/$Al_2O_3$ bilayer nanofilm, leveraging a medium-entropy carbonitride as a robust refractory plasmonic material. The (TiZrHf)$C_xN_y$ absorber layer self-assembles into a distinctive nanocomposite structure, with 2–3 nm crystalline nanoparticles embedded in an amorphous matrix. This structure enables intense and broadband solar absorption via the Localized Surface Plasmon Resonance (LSPR) effect, achieving a high solar absorptance. Concurrently, the SSA exhibits a low thermal emittance, ensuring minimal heat loss. Crucially, the SSA demonstrates exceptional thermal stability, with its optical properties remaining virtually unchanged after annealing at 400 °C in air for 10 h.

## 1. Introduction

The escalating global energy demand has positioned solar-to-thermal conversion technologies, particularly concentrated solar power (CSP), as a critical pathway toward achieving carbon neutrality [1–4]. The performance of solar selective absorbers (SSAs), which are the key components of these systems, is of paramount importance. An ideal SSA must maximize solar absorptance across the solar spectrum (0.3–2.5 μm) while simultaneously minimizing thermal emittance in the infrared region (>2.5 μm) [5]. However, the development of SSAs that concurrently exhibit high spectral selectivity, long-term thermal stability, and cost-effectiveness remains a huge challenge.

Dielectric-metal nanocomposites incorporating plasmonic metals such as Cu, Ag, and Al exhibit exceptional capabilities for sunlight absorption, primarily due to their pronounced localized surface plasmon resonance (LSPR) effect [6,7]. Broadband solar absorption can be achieved by precisely tailoring the size, morphology, and distribution of the metallic nanoparticles [8]. However, the practical application of these materials is hindered by inadequate thermal stability, a consequence of the low melting points of the constituent metals. Our strategy to address this issue involves the introduction of transition metal carbonitrides, particularly those from Group IV elements (Ti, Zr, and Hf), as absorbing layers. The constituent nitrides of this system (e.g., TiN, ZrN, and HfN) not only exhibit LSPR effect comparable to noble metals but also possess the characteristics of ultrahigh-temperature ceramics (melting points ≥ 2900 °C), providing exceptional thermal stability and chemical inertness [9–11]. Furthermore, by tuning the C/N ratio, these carbonitride films can be engineered to form self-assembled nanocomposite structures. These unique characteristics are anticipated to synergistically yield outstanding performance in solar-to-thermal conversion applications.

This study aims to demonstrate that the (TiZrHf)$C_xN_y$/$Al_2O_3$ bilayer nanofilm, comprising a medium-entropy carbonitride absorber layer and an $Al_2O_3$ antireflection layer, achieves not only high spectral selectivity but also superior thermal stability. This innovative design presents a robust and cost-effective solution, serving as a blueprint for the development of next-generation SSAs.

* Corresponding author at: School of Materials and Engineering, Jiangsu Key Laboratory for Advanced Metallic Materials, Southeast University, Nanjing 211189, China.
** Corresponding authors.
*E-mail addresses:* jing_zhiyuan@163.com (Z. Jing), qwang678@seu.edu.cn (Q. Wang), liangxb_d@163.com (X. Liang).

https://doi.org/10.1016/j.matlet.2026.140062
Received 22 October 2025; Received in revised form 11 December 2025; Accepted 5 January 2026
Available online 6 January 2026

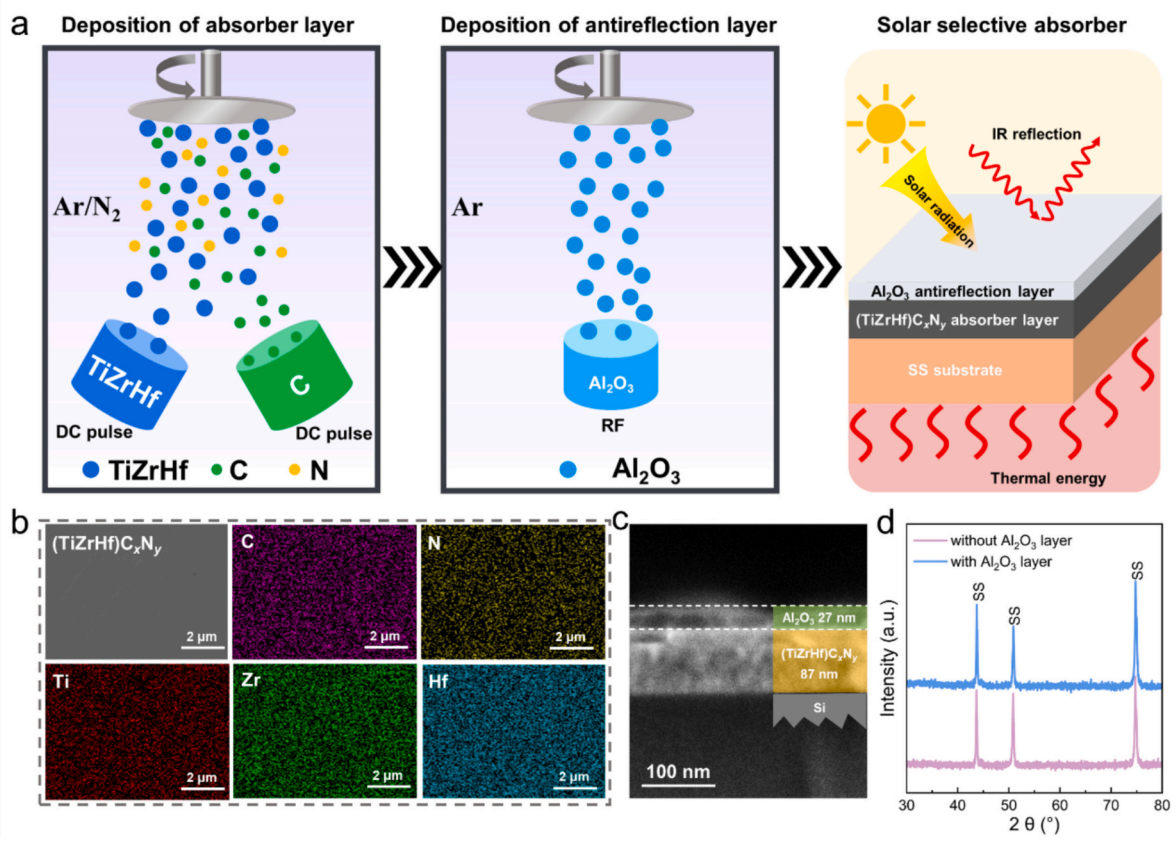


**Fig. 1.** (a) Schematic illustration of the two-step deposition process for the (TiZrHf)$C_xN_y$ absorber layer and the $Al_2O_3$ antireflection layer, along with the working principle and structural diagram of the as-designed SSA. (b) Surface SEM image and the corresponding EDS mapping of the single (TiZrHf)$C_xN_y$ absorber layer. (c) The cross-sectional SEM image of (TiZrHf)$C_xN_y$/$Al_2O_3$ bilayer nanofilm deposited on Si substrate. (d) XRD patterns of the (TiZrHf)$C_xN_y$ absorber layer with and without the $Al_2O_3$ top layer on a SS substrate.

## 2. Experimental

A (TiZrHf)$C_xN_y$ absorbing layer and an $Al_2O_3$ antireflection layer were sequentially deposited on 304 stainless steel (SS) using a co-sputtering system (Fig. 1a). The equimolar TiZrHf target (99.95 %) and graphite target (99.99 %) were powered by direct current (DC) pulsed power, whereas the $Al_2O_3$ target (99.99 %) was powered by radio-frequency (RF) power. To remove the surface impurity, all substrates were ultrasonically cleaned in absolute ethanol for 15 min. Prior to deposition, the base pressure of deposition chamber was pumped to 4 $\times$ $10^{-4}$ Pa by turbomolecular pump and the substrates were heated to 300 °C. During the deposition of the absorbing layer, high-purity Ar and $N_2$ were introduced into the chamber, with flow rates maintained at 40 sccm and 1.5 sccm, respectively. For the deposition of the anti-reflection layer, only high-purity Ar was introduced into the chamber, with a flow rate maintained at 65 sccm. The absorbing layer and anti-reflection layer were deposited at constant work pressure of 0.5 Pa and 1.0 Pa, respectively. The sputtering currents applied to the TiZrHf and graphite targets were 0.4 A and 0.5 A, respectively, while the sputtering power for the $Al_2O_3$ target was set at 100 W.

The reflectance spectra in the wavelength range of 0.3 to 2.5 μm were obtained using a Cary 5000 UV–vis-NIR spectrometer. The IR reflectance measurements were conducted with a FTIR spectrometer (Thermo Scientific Nicolet iS50R) over a spectral range of 2.5 to 20 μm. X-ray diffraction (XRD) patterns were recorded on a D8-Discover diffractometer utilizing Cu K$\alpha$ ($\lambda$ = 1.541 Å) radiation. The surface and cross-sectional morphology of the films was observed using a field emission scanning electron microscope (SEM, Nova Nano SEM450). Additionally, the nanostructure of the absorber layer was further investigated in detail using transmission electron microscopy (TEM, Talos F200X).

## 3. Results and discussion

As illustrated in Fig. 1a, the designed SSA is composed of an absorber layer (TiZrHf)$C_xN_y$ and an antireflection layer $Al_2O_3$ on a SS substrate. The surface SEM image and corresponding EDS mapping of the absorber layer reveals a smooth surface morphology and homogeneous

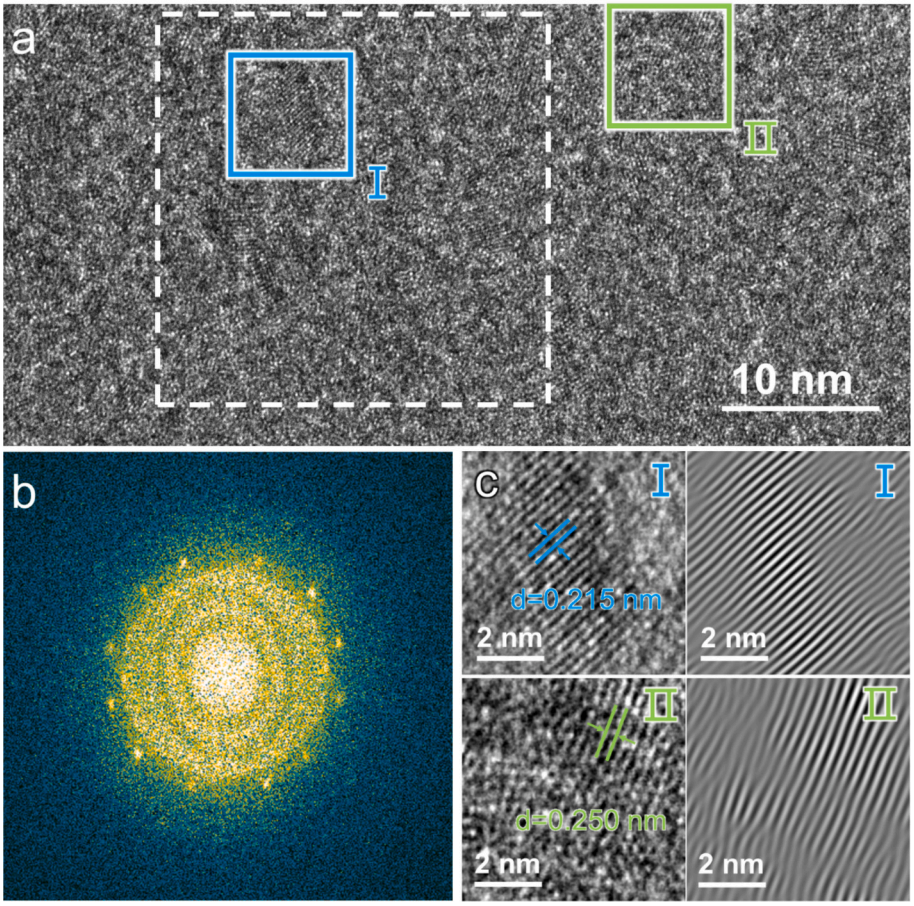


**Fig. 2.** (a) High-resolution transmission electron microscopy (HRTEM) image of (TiZrHf)$C_xN_y$ absorber layer. (b) The corresponding Fast Fourier Transform (FFT) pattern taken from the white dashed square in (a). (c) Magnified HRTEM images of the nanocrystalline regions labeled I and II in (a), and their corresponding Inverse Fast Fourier Transform (IFFT) images.

distribution of all constituent elements (Fig. 1b). The quantitative analysis of the EDS mapping indicates a metal-to-non-metal element ratio of 1:9 (Fig. S1). Fig. 1c shows that the thicknesses of (TiZrHf)$C_xN_y$ absorber layer and $Al_2O_3$ antireflection layer are 87 nm and 27 nm, respectively. The samples both with and without the $Al_2O_3$ antireflection layer exhibit only diffraction peaks corresponding to the SS substrate (Fig. 1d), which indicates that both the (TiZrHf)$C_xN_y$ absorber and the $Al_2O_3$ antireflection layer predominantly possess an amorphous or nanocomposite structure.

The HRTEM image of the (TiZrHf)$C_xN_y$ layer (Fig. 2a) reveals 2–3 nm nanocrystalline clusters embedded in an amorphous matrix. This characteristic is a distinctive feature of nanocomposite materials, consisting of a nanocrystalline metal carbonitride phase and an amorphous carbon matrix, commonly observed in metal carbonitride thin films prepared via magnetron sputtering [12]. Based on the refractory plasmonic properties of transition metal nitrides and carbonitrides, the (TiZrHf)$C_xN_y$ film is a novel plasmonic nanocomposite material. The self-assembly of such nanocomposite structure is governed by a synergy between thermodynamic driving forces and the kinetic limitations of the magnetron sputtering process [12]. The FFT pattern of the selected area (Fig. 2b) marked by the white square in Fig. 2a, characterized by broad and diffuse halos alongside sharp spots, further demonstrates the nanocomposite structure. Detailed analysis of regions I and II (Fig. 2c, left panels) shows lattice fringes with d-spacings of 0.250 nm and 0.215 nm, corresponding to the (111) and (200) crystal planes of the face-centered cubic (TiZrHf)$C_xN_y$ solid solution, respectively. The IFFT images (Fig. 2c, right panels) reveal significant lattice distortion, which arises from the atomic size mismatch.

The digital photograph (Fig. 3a) illustrates the semi-transparent nature of the (TiZrHf)$C_xN_y$ absorber layer. The transmission spectrum (Fig. 3b) demonstrates an intense and broad absorption band across the visible and near-infrared regions, which is indicative of LSPR arising

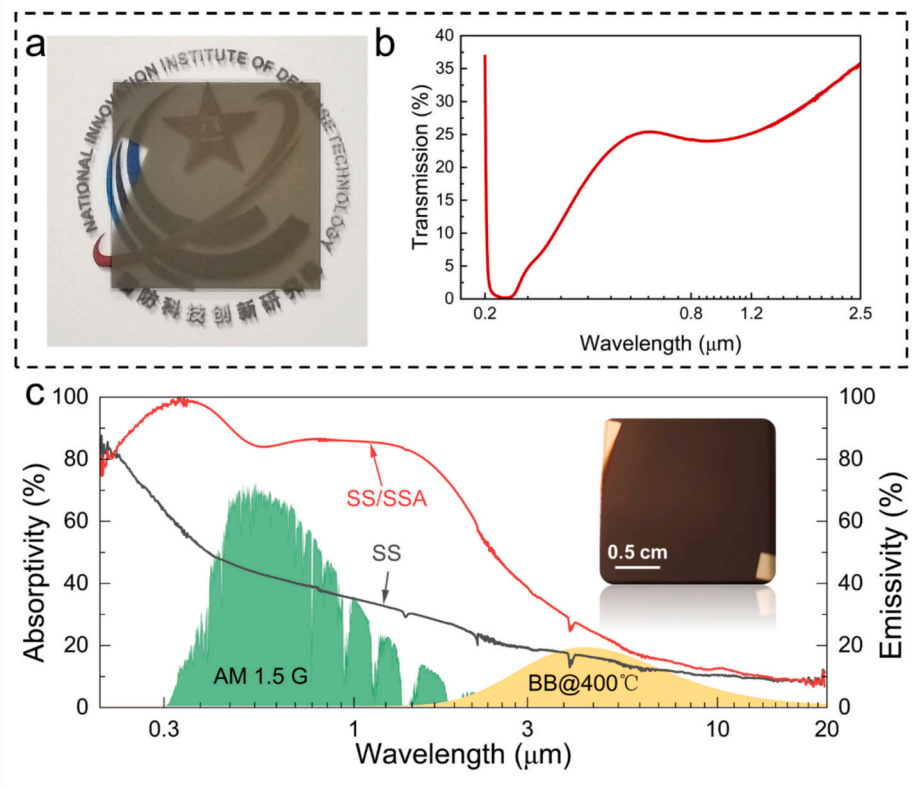


**Fig. 3.** (a) A digital photograph and (b) the corresponding transmission spectrum of the semi-transparent (TiZrHf)$C_xN_y$ film deposited on a glass substrate. (c) Spectral absorptivity of the SS/SSA and bare SS substrate. The inset is a digital photograph of the final SS/SSA sample.

from the plasma nanocomposite structure (Fig. 2) [7,13]. As depicted in Fig. 3c, the SSA simultaneously achieves a high solar absorptivity ($\alpha$ = 85.6 %) and a low thermal emittance ($\varepsilon$ = 11.3 %), effectively facilitating solar heating. Although some state-of-the-art SSAs achieve slightly higher absorptance (see Table S1), our SSA demonstrates competitive optical performance with a significantly simpler bilayer structure and enhanced oxidation resistance.

The thermal stability and heat-suppression capability of the optimized SSA are evaluated. Fig. 4a illustrates the experimental setup, where the SSA, SS substrate, and high-emissivity silicon wafer are simultaneously heated to 400 °C for 10 h, with their surface radiation temperatures monitored using an IR camera. As shown in Fig. 4b, the spectral reflectance curves of the SSA before and after the prolonged heating test are nearly identical. Extending the annealing time to 24 h yielded similar stability (Fig. S2). This result indicates that the nanocomposite structure and its associated plasmonic absorption properties exhibit high stability, likely due to the sluggish-diffusion effect of medium-entropy materials and the high melting point of ceramic materials [4,5]. Furthermore, the low-emissivity performance, crucial for minimizing heat loss, was confirmed in the long-term heating experiment presented in Fig. 4c. The SSA consistently maintains a significantly lower radiation temperature of approximately 170 °C, comparable to that of the bare SS substrate. This notable temperature difference is a direct consequence of the SSA's low thermal emissivity in the infrared spectrum. The infrared thermal images provide striking visual confirmation of this effect. The stable, low radiation temperature over the entire 10 h test period robustly demonstrates the coating's excellent potential for practical high-temperature solar-thermal applications.

## 4. Conclusion

In summary, we have successfully designed and fabricated a high-performance solar selective absorber based on a novel bilayer nanofilm consisting of (TiZrHf)$C_xN_y$ and $Al_2O_3$. The core of this design is the medium-entropy (TiZrHf)$C_xN_y$ layer, which is a refractory plasmonic nanocomposite. Its unique microstructure, characterized by nanocrystallites dispersed within an amorphous matrix, induces a strong Localized Surface Plasmon Resonance effect, leading to excellent solar absorptance across the solar spectrum. Moreover, the inherent sluggish diffusion effect and high melting point of the medium-entropy ceramic confer outstanding stability to the absorber, exhibiting negligible degradation after prolonged annealing at 400 °C in air.

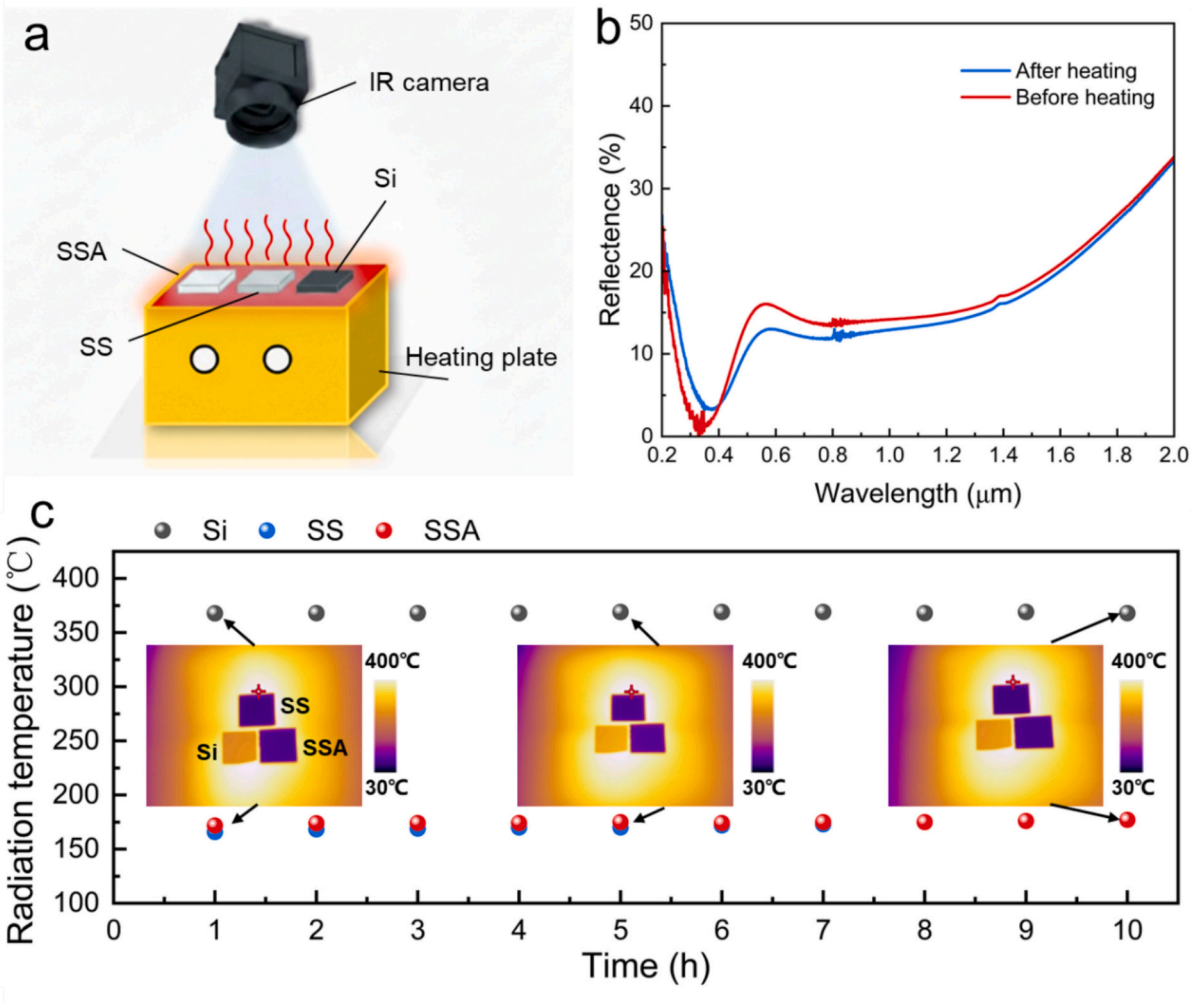


**Fig. 4.** (a) Schematic diagram of the experimental setup used for high-temperature testing. (b) Spectral reflectance of the SSA before and after annealing at 400 °C for 10 h in air. (c) Surface radiation temperatures of the SSA, SS substrate, and Si wafer. The insets show the corresponding IR thermal images at selected time intervals.

## CRediT authorship contribution statement

**Gaopeng Zou:** Writing – review & editing, Writing – original draft, Methodology, Formal analysis. **Yuxi Qi:** Methodology. **Zhiyuan Jing:** Supervision, Methodology, Investigation. **Zhibin Zhang:** Methodology, Formal analysis. **Qianqian Wang:** Supervision, Methodology, Investigation. **Zhenfeng Hu:** Methodology, Investigation. **Xiubing Liang:** Supervision, Methodology, Formal analysis. **Baolong Shen:** Supervision, Methodology.

## Declaration of competing interest

The authors declare that they have no known competing financial interests or personal relationships that could have appeared to influence the work reported in this paper.

## Acknowledgements

This research did not receive any specific grant from funding agencies in the public, commercial, or not-for-profit sectors.

## Appendix A. Supplementary data

Supplementary data to this article can be found online at https://doi.org/10.1016/j.matlet.2026.140062.

## Data availability

Data will be made available on request.

## References

[1] B. Liu, C. He, Y. Li, Z. Li, W. Wang, Z. Lu, Z. Wang, S. Zhao, G. Liu, X. Gao, Matter 7 (2024) 140–157.
[2] C.Y. He, P. Zhao, X.H. Gao, G. Liu, P.Q. La, Mater. Lett. 329 (2022) 133198.
[3] N. Suwannakham, A. Tubtimtae, Mater. Lett. 336 (2023) 133920.
[4] P. Zhao, M. Dong, X. Liu, Y. Wang, W. Wang, B. Liu, Z. Lu, C. He, X. Gao, Adv. Funct. Mater. 34 (2024) 2411316.
[5] Y. Li, C. Lin, Z. Wu, Z. Chen, C. Chi, F. Cao, D. Mei, H. Yan, C.Y. Tso, C.Y.H. Chao, B. Huang, Adv. Mater. 33 (2021) e2005074.
[6] M.A. Assad, M. Abdelaziz, T. Hartig, T. Strunskus, A. Vahl, F. Faupel, M. Elbahri, Adv. Mater. 37 (2025) 2501080.
[7] J. Drewes, N. Perdana, K. Rogall, T. Hartig, M. Elis, U. Schürmann, F. Pohl, M. Abdelaziz, T. Strunskus, L. Kienle, M. Elbahri, F. Faupel, C. Rockstuhl, A. Vahl, Part. Part. Syst. Charact. 41 (2024) 2300102.
[8] M.A. Assad, M. Elbahri, Adv. Funct. Mater. 35 (2025) 2418271.
[9] P. Das, B. Biswas, K.C. Maurya, M. Garbrecht, B. Saha, ACS Appl. Mater. Interfaces 14 (2022) 46708–46715.
[10] H. Reddy, U. Guler, Z. Kudyshev, A.V. Kildishev, V.M. Shalaev, A. Boltasseva, ACS Photon. 4 (2017) 1413–1420.
[11] U. Guler, A. Boltasseva, V.M. Shalaev, Science 344 (2014) 263–264.
[12] O. Wilhelmsson, M. Råsander, M. Carlsson, E. Lewin, B. Sanyal, U. Wiklund, O. Eriksson, U. Jansson, Adv. Funct. Mater. 17 (2007) 1611–1616.
[13] M.K. Hedayati, M. Javaherirahim, B. Mozooni, R. Abdelaziz, A. Tavassolizadeh, V. S.K. Chakravadhanula, V. Zaporojtchenko, T. Strunkus, F. Faupel, M. Elbahri, Adv. Mater. 23 (2011) 5410–5414.